東京大学 大学院新領域創成科学研究科
基盤科学研究系
先端エネルギー工学専攻

平成 25 年度

修士論文

Influence of the ambient gas content on the propagation properties of laser supported detonation wave: A case study on Argon and Nitrogen gases

－　雰囲気ガスがレーザー支持爆轟波の伝播特性に与える影響:アルゴンと窒素の比較－

2014 年 1 月提出
指導教員　小紫　公也　教授

47126068　Ofosu Joseph Ampadu

Graduate School of Frontier Sciences, The University of Tokyo

Transdisciplinary Sciences, Department of Advanced Energy

2013-2014

Master's Thesis

Influence of the ambient gas content on the propagation properties of laser supported detonation wave: A case study on Argon and Nitrogen gases

Submitted January, 2014

Supervisor: Professor Komurasaki Kimiya

47126068 Ofosu Joseph Ampadu

Abstract

Laser propulsion technology is potentially capable of influencing the design of rockets with an advantageous combination of the requisite performance characteristics such as high specific impulse and high thrust as well as low propulsion weight since the source of energy need not be carried on-board. Hence, as a beamed energy propulsion concept and a future propulsion system, it is vital to understand the sustenance and termination conditions of the laser supported detonation (LSD) wave, which enhances efficient thrust generation.

In this study, different ionization front velocities of different gas species namely: Air, Argon (Ar) and Nitrogen (N_2), were experimentally observed with respect to laser intensity per unit density. The aim of the study was to predict the LSD wave velocity prior to its termination using a 1-D radiative hydrodynamic model. Thus estimated ionization front velocities (obtained from the 1-D radiative model and measured parameters) were compared with measured ionization front velocities in Ar and N_2. The rationale was to compare a monoatomic and a diatomic gas. The diagnostics tools used were two-wavelength Mach-Zehnder interferometry and optical emission spectroscopy.

The model predicted the LSD wave velocities precisely in terms of tendency but not accurately. This is due to the dimensional, translational ionization frequency and molecular ionization assumptions of the model. The computed flux and corresponding estimated front seed electron number density in both Ar and N_2 indicated and further validated the applicability of the model to other gases by corroborating measured results.

Acknowledgement

I am first and foremost thankful to the Almighty God for the gift of life and health.

I am also very grateful and thankful to Professor Kimiya Komurasaki for the fatherly and academic supervisory role he meted out during the period of study. My next gratitude goes to Associate Professor Koizumi Hiroyuki and Dr. Tony Schoenherr for their insightful critique, guidance and assistance in my studies at The University of Tokyo.

I am also thankful to Kohei Shimamura for his immense contribution and advice in my academic learning process. My heartfelt thanks is to all members of the Komurasaki laboratory of the Advanced Energy and Aeronautics & Astronautics departments.

Last but not least I am thankful to my parents, siblings, loved ones and all my friends for seeing me through every step of my journey. Especially, I cannot overemphasize the encouragement, support and counsel of my brother Mr Stephen K. B. Omane.

Finally, I am also grateful for the Ministry of Education, Culture, Sports, Science and Technology (MEXT [MONBUKAGAKUSHO]) Scholarship, without which I would not have been able to pursue this academic program in Japan.

Joseph Ampadu Ofosu

January 31, 2014.

Table of Contents

List of Figures

List of Tables

Nomenclature

A : complex amplitude of vibration
A_{ik} : transitional probability
a : amplitude
c : speed of light in vacuum
d : width of test section or LSD phenomenon
E : electric field
E_i : excitation energy at level i
e : electron charge magnitude
g_i : statistical weight
h : Planck constant/ number of fringe shifts
I : optical intensity/ radiated power per unit volume
I_{ik} : integrated line intensity
I_{sp} : specific impulse
i_ν : radiation due to free-free and free-bound transitions
K_j : relative refractive index of species j
k : wave propagation constant or wave number
k_B : Boltzmann constant
l_{coh} : coherence length
M : Mach number
m_e : electron mass
N : refractive index
n_{co} : cut-off density
n_e : electron number density
n_j : number density of species j
p : optical path difference
q : heat deposition
T : period of vibration
T_e : electron temperature
T_{ex} : electron excitation temperature
t_{coh} : coherence time
U : detonation wave velocity
U_j : internal partition function of species j
v : speed of wave in a medium
z : displacement
γ : ratio of specific heats/ fringe contrast
ε_o : permittivity of free space
ϵ : dielectric constant
κ : photon-absorption coefficient
λ : wavelength
λ_{mfp} : mean free path of photon-absorption

λ_n : wavelength in a medium
ν : frequency
ν_i : ionization frequency
ξ_{12} : coherence factor for two beams superposed at point p
ρ : density
τ_d : tail decay constant of CO_2 laser
ϕ : phase difference/ photon flux
Ω : solid angle
ω : angular frequency
ω_{pe} : electron plasma frequency

Subscripts
i : upper energy level
k : lower energy level

Chapter 1

INTRODUCTION

1.1 Background

This section gives a brief overview on the subject of laser propulsion: its history and some research status. The advantageous characteristics of laser propulsion system as a beamed energy propulsion concept compared with the conventional chemical rocket system are presented.

1.1.1 Chemical rocket systems

The relative affordability and reliability of conventional chemical rocket systems has made them the most dependable way of reaching the outer space despite their expensiveness. The typical launch cost is about $ 5,000 per kilogram for low earth orbit (LEO) and up to about $ 15,000 per kilogram for geostationary transfer orbit (GTO)[1)]. Moreover, due to the fact that a higher fraction of the launch mass is fuel, the payload is limited as well.

Proposals have been made that could help solve the high cost and payload limitation of today's rocket systems. These include but are not limited to the mass driver method where: 1) high speed acceleration of a projectile is achievable by the application of electromagnetic force on a path[2)-3)] and 2) the acceleration of a vehicle by a remotely transmitted laser power, termed as laser propulsion[4)]. Both of these do not require an on-board energy source.

1.1.2 Laser propulsion

In 1972, Kantrowitz was the first to propose a propulsion system powered by a high-power ground-based laser[4]. This system, considered as one of the beamed energy propulsion (BEP) concepts is a resource saving alternative to chemical rocket systems with cost minimisation capabilities and low emission. Infinite specific impulse I_{sp} is attainable in an air-breathing flight mode within the earth's atmosphere where no fuel is required on board. It is also possible for the laser propulsion vehicle to go directly to geosynchronous orbit (GEO) without parking in LEO[5]. Gas is laser heated instead of combusted, thus vehicle structure is expected to be simple and relatively cheap as there would be no need of pressure vessel or turbo-pump systems. In contrast, the laser equipment required for the energy beaming and which is expected to be much higher than the launch cost is easily accessible, maintainable and replaceable as it is situated here on earth or in a space-based station. With a space-based laser equipment, the in-space laser propulsion system proposed by Minovich[6] is expected to achieve a relatively higher specific power than that of solar electric propulsion.

Depending on the mode of laser transmission, laser propulsion is categorized as continuous wave (CW) or repetitively pulsed (RP). In CW laser propulsion, a stable laser discharge plasma known as laser sustained plasma (LSP) is confined away from the chamber wall and maintained by the inverse bremsstrahlung (IB) process. Thus the propellant gas is heated to a higher temperature resulting in a relatively higher I_{sp} than that of chemical rocket systems. CW laser is a candidate for in-space propulsion since the current power levels of this device in the several kW rating, is insufficient for ground to space launch applications. In RP laser propulsion, pulsed laser irradiation ablates the surface of a target, termed as laser ablation, or focused laser beam breaks down an ambient gas such as air to produce plasma. The formation of plasma by this way is called laser induced plasma (LIP). The latter mode of plasma formation via the breakdown of air is termed air-breathing RP laser propulsion. Due to its MW class

rating, the RP laser is a suitable candidate for launch applications. The highway of light and beam riding concepts make long distance tracking and beam pointing to vehicles unnecessary[7]. Different forms of the laser propulsion concept have been proposed: flat plate[8], pulsejet[8] and the laser in-tube accelerator (LITA) [9]. These are schematically shown in Figure 1.1. Also, with the use of on-board diode lasers whose power supply source is an array of solar panels, laser microthrusters[10] have been proposed as a candidate for precise orbital positioning and attitude control of microsatellites.

1.2 Laser Detonation System

1.2.1 Laser detonation thruster

Laser detonation thrusters are expected to have a comparatively higher payload ratio since no or less propellant mass is required during atmospheric flight. Thrust is applied to the bottom of the vehicle when the focused laser beam creates laser detonation waves which reflect off the inner wall of the vehicle as blast waves. A refilling of air takes place after the exhaust of the heated gas during the laser pulse interval, and the cycle is referred to as the pulsed detonation engine (PDE, Figure 1.2 [11]) cycle.

(a)

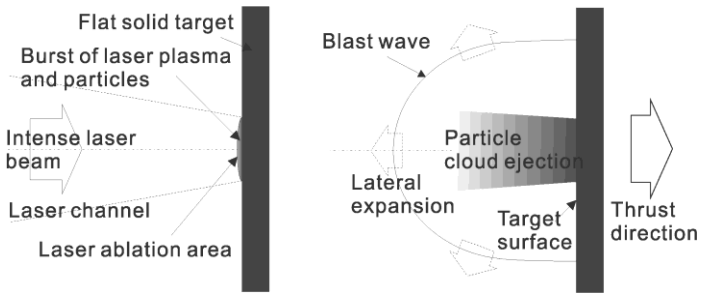

(b)

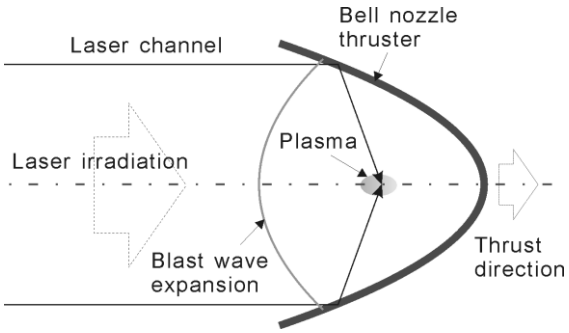

(c)

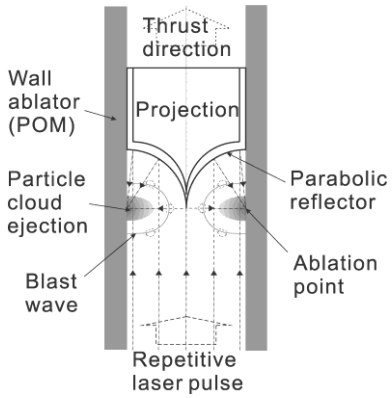

Figure 1.1 Proposed forms of laser propulsion concept: (a) flat type[8], (b) Pulsejet[8] and (c) LITA.[9]

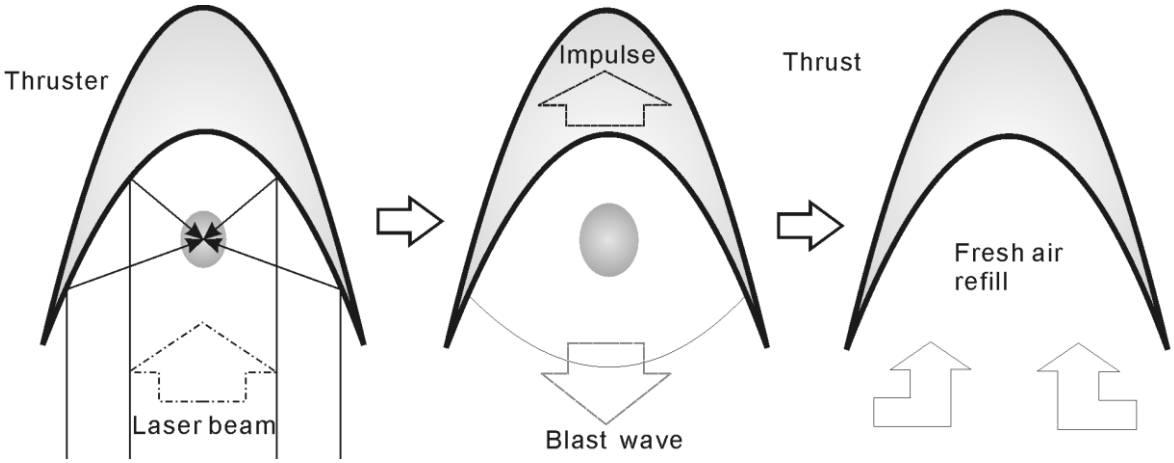

Figure 1.2 PDE cycle (from left to right: beam focusing and gas breakdown, plasma formation to blast wave expansion and thrust generation, refill of fresh air).[11]

Three modes of flight operation of an air-breathing laser propulsion system have been proposed[5]. The first is the pulsejet mode which takes place in an altitude range of 0 ~ 7 km where air is the propellant gas. The second is the ramjet mode within the range of 7 ~ 40 km at which air is taken in from the vehicles front and compressed for ignition or breakdown. The last is the rocket mode at an altitude beyond 40 km. In this mode an on-board propellant gas such as argon is used for thrust generation due to the less dense ambient conditions.

1.2.2 Laser supported detonation (LSD)

When a pulsed laser beam is focused, breakdown occurs after the ionization potential of the ambient gas content is exceeded. The induced plasma formed as a result of the breakdown process absorbs the irradiated laser energy in two regimes: LSD regime and the laser supported combustion (LSC) regime. During the LSD regime, the typical laser intensity is higher than 100 GW/m^2 [12] and the laser energy is absorbed in a post shock plasma layer. The plasma is heated isometrically and the shock wave is efficiently enhanced resulting in the generation of a great thrust. In the LSC regime, the typical intensity is less than 10 GW/m^2 [12]; thus the shock front and the plasma front travel separately (Figure 1.3). In this case, the absorption of laser energy occurs in the plasma behind the shock wave, the plasma is heated isobarically and no additive energy for thrust generation is expected. The transition from LSD to LSC affects the thrust performance of RP laser propulsion. Thus it is imperative to understand the physics of LSD and its sustenance or the heating regime transitions, since the laser intensity on a wave front decreases with time due to the decaying laser pulse shape and increasing beam cross section area of focusing optics.

The propagation mechanism of the LSD structure is represented in Figure 1.4[13] and is briefly described. The photon energy hv radiated from the plasma is absorbed by the

ambient gas, in this case Argon, ahead of the shock front. This leads to the generation of a seed electron in a process believed to be photoionization, and occurs when the radiated energy exceeds the ionization potential. The generation of the seed electron is not considered to be the effect of shock compression. The seed electron is further accelerated by the IB process and this leads to avalanche ionization increasing the electron number density ahead of the shock front. When the characteristics length of the ionization regime is equivalent to the Debye length, a LIP is formed[14)-15)]. This creates the precursor which further acts as an absorption wave ahead of the shock wave during the LSD regime.

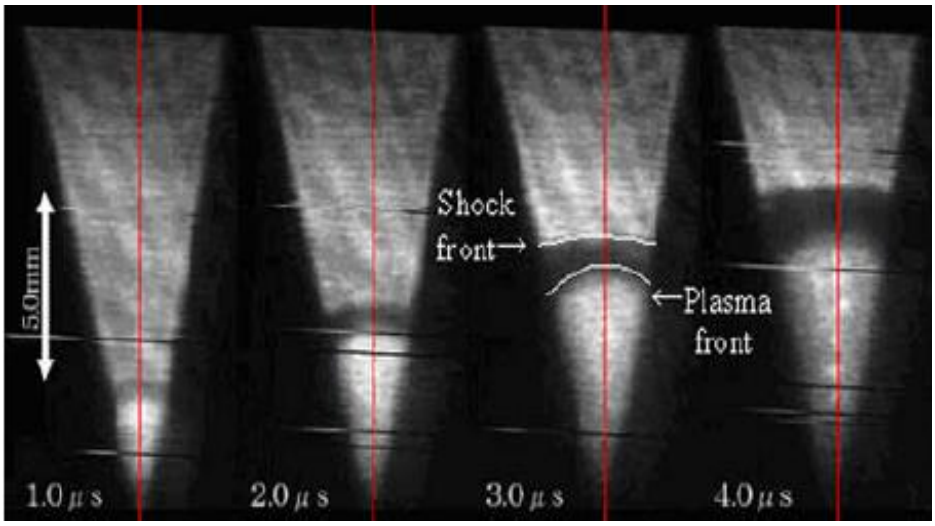

Figure 1.3 Shadowgraphs depicting the LSD and LSC regimes.[12)]

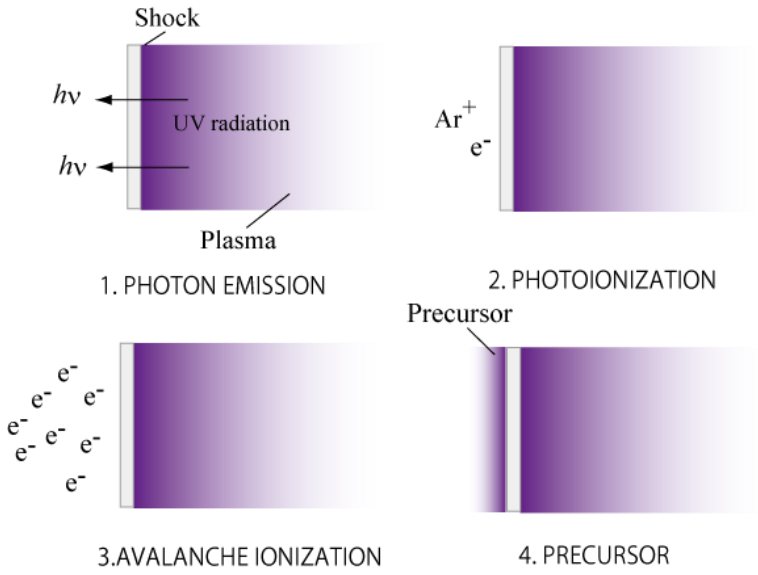

Figure 1.4 Propagation mechanism of LSD wave.

1.3 Previous Studies

Raizer[16] proposed that LSD terminated when the energy used to drive the lateral wave expansion is equivalent to that of the front wave expansion in a cylindrical laser channel. The influences of the focusing f number[17], ambient pressure[18] and laser power density[19] on LSD termination have been investigated by Mori.

Ushio et al[12] investigated Raizer's effect quantitatively by a line focused laser beam, and it was observed that the lateral expansion from the LSD region to the ambient air was reduced by mechanically restricting the wave expansion in quasi-1D space using a wedged nozzle. As a result, the measured threshold laser intensity for LSD termination in the quasi-1D confined configuration was about half that of the 2D unconfined configuration. The velocity of the LSD wave in quasi-1D was faster than that in 2D. Thus these confinement geometries have an influence on the energy dissipation mechanism such as ionization and radiation during the LSD wave propagation. Their results are shown in Table 1.1.

Table 1.1 LSD termination conditions.[12)]

Parameters	**Dimension of phenomena**	
	2D unconfined	**Quasi-1D confined**
time (μs)	1.2	1.8
Laser threshold intensity (GW/m^2)	34	17
Mach number	5.3	6.3

Shimamura et al[20)] studied the distribution of electron density, in atmospheric air using the two-wavelength Mach-Zehnder interferometer. Per their analyses, it was found that the density distribution at the shock front was non-zero. This distribution at an elapsed time of 1.2 μs is shown in Figure 1.5.

1.4 Research Objectives

Numerous research and extensive experimental analyses have demonstrated that laser propulsion is the candidate with performance characteristics midway/ between those of chemical and electrical propulsion systems[21)]. Laser propulsion eliminates the deficiency of both chemical and electrical systems, namely: low I_{sp} and low thrust respectively. In the year 2000, the longest laser-powered free flight of 12.7 s and an altitude record of 71 m were achieved. This was accomplished with a 12 cm diameter model of the lightcraft using a 10 kW CO_2 pulsed laser[22)]. The feasibility of these experimental results motivates a further investigation into the structure and characteristics of LSD, which includes but not limited to electron number density n_e and electron temperature T_e, as well as velocity of the ionization front wave.

A preliminary result of this study showed different characteristics in the ionization front velocities of different gas species under different laser intensity per unit density (laser intensity is used for laser intensity per unit density in this study). This is shown in Figure 1.6. At high laser irradiation, the velocity profiles were different in all gases and exhibited a weak overdriven detonation phenomenon. However in the low laser

intensity zone (Region of Interest), the speeds were similar. The region prior to and termination of LSD was designated as the region of interest. This is due to the significance of understanding the sustenance or termination conditions of LSD, since its termination simply means inefficient transfer of energy for propulsion. The study of ambient gas influence on the LSD propagation properties is indispensable, since in the rocket mode, an on-board propellant would be vital for continuous propulsion.

Raizer's[23] theory of detonation is inadequate to describe the phenomenon observed in our experiments. This is because the theory assumes the existence of a shockwave for detonation to occur; in other words, detonation is shockwave induced. The theory is simply based on the conservation of mass, momentum and energy. The straight line depicted in the graph of Figure 6 is the Chapman-Jouguet line at a given ratio of specific heats. This is the limiting velocity line without which detonation cannot occur. The plasma propagation phenomenon observed in our experiments is a radiative induced phenomenon and thus photoionization and absorption play a significant role. Thus discharge-based physics is required to explain the generation and propagation process of the plasma's constituent microscopic particles such as electrons.

The aim of this thesis was to predict the LSD wave velocity prior to its termination using a 1-D radiative hydrodynamic model[24]. The model stipulates that ionization front velocity is a function of ionization frequency and the number of seed electrons at the front of the shockwave is a function of the UV flux radiated from the plasma. The model also assumes molecular ionization only (i.e. $N_2 + e^- \Rightarrow {N_2}^+ + 2e^-$). The approach was to compare measured velocities from experiment with estimated velocities (obtained from the 1-D radiative model[24] and measured parameters). The diagnostics tools used were two-wavelength Mach-Zehnder interferometry and optical emission spectroscopy.

The objectives of this thesis are summarized as follows:

- Profile electron number density distribution in Argon (Ar) and Nitrogen (N_2) gases.
- Obtain electron excitation temperature in Ar and N_2 gases.
- Obtain the ionization front speeds in Ar and N_2 using shadowgraph experiment.
- Analytically estimate the ionization front speeds in Ar and N_2 using the 1-D radiative hydrodynamic model by Shimamura[24] together with measured parameters obtained from experiment.

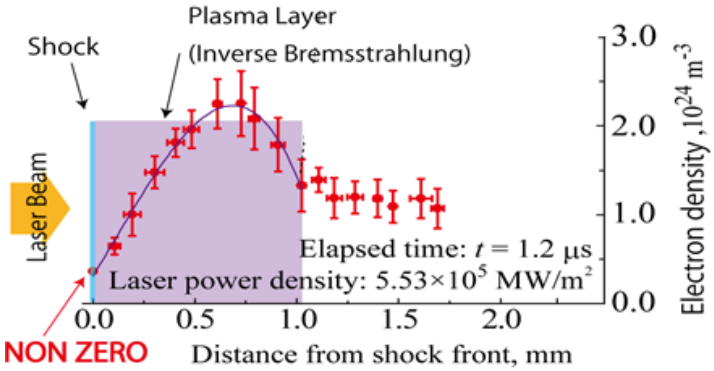

Figure 1.5 Electron number density distribution in air.[20]

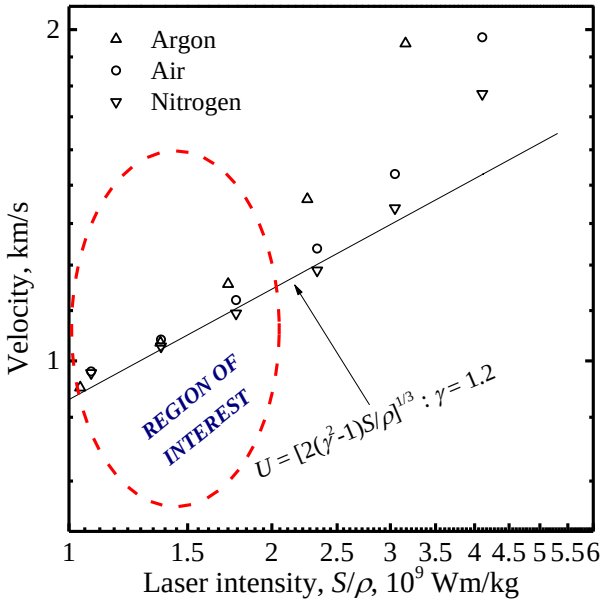

Figure 1.6 A plot of ionization front velocities versus laser intensity.

1.5 Thesis Structure

This chapter briefly presented the background and concepts of laser propulsion system as a future propulsive system. Also the aims and objectives of this thesis are given here.

In Chapter 2, basic interferometric theory and conditions for fringe pattern formation such as coherence are discussed. The basic processes of deducing electron number density and electron excitation temperature distribution are presented as well.

Chapter 3 briefly describes the apparatus and specifications of the equipment used in this study.

Chapter 4 discusses the results obtained in this study.

Chapter 5 concludes on the findings of this study.

References

1) Wertz, J., and Larson, W.: Reducing Space Mission Cost, *Kluwer Academic Publishers*, Boston, 1996.
2) Berning, P.R., Hummer, C. R., and Hollandsworth, C. E.: A coilgun-based launch system, *IEEE Transactions on Magnetics*, **35**, 1, pp. 136-141.
3) Parker, J. V.: Electromagnetic projectile acceleration utilizing distributed energy sources, *Journal of Applied Physics*, **53,** 10 (1982), 6710.
4) Kantrowitz, A.: Propulsion to Orbit by Ground-Based Lasers, *Astronautics & Aeronautics*, **10** (1972), pp. 74-76.
5) Katsurayama, H., Ushio, M., Komurasaki, K., and Arakawa, Y.: Feasibility for the Orbital Launch by Pulse Laser Propulsion, *Journal of Space Technology and Science*, 20, 2 (2005), pp. 32-42.
6) Minovich, M. A.: Reactorless Nuclear Propulsion – The Laser Rocket, AIAA paper 72-1095, *AIAA/SAE 8th Joint Propulsion Specialist Conference*, December 1972.
7) Myrabo, L. N.: "Highways of Light", *The Future of Space Exploration* by Scientific American, 1999, pp.66-67.
8) Toyoda, K., Komurasaki, K., and Arakawa, Y.: Thrust Performance of a CW Laser Thruster in Vacuum, *Vacuum*, **65**, 3-4 (2002), pp. 383-388.
9) Sasoh, A., Jeung, I.S., and Choi, J.Y.: Access to Space without Energy and Propellant on Board, *Beamed Energy Propulsion: Fifth International Symposium on Beamed Energy Propulsion*, AIP Conference Proceedings, **997** (2007), pp. 37- 46.
10) Phipps, C.R., Luke, J.R., Helgeson W., and Johnson, R.: Performance Test Results for the Laser-Powered Microthruster, *Beamed Energy Propulsion: Fourth International Symposium on Beamed Energy Propulsion*, AIP Conference Proceedings, **830**, May 2, 2006, pp. 224-234.
11) Wang, B.: Laser Detonation Propulsion with solid-state Laser, *Graduation Thesis*, The University of Tokyo, March 2012, p. 12.
12) Ushio, M., Komurasaki, K., Kawamura, K. and Arakawa, Y.: Effect of laser supported detonation wave confinement on termination conditions, *Shock Waves*, **18** (2008), pp. 35-39.
13) Shimamura, K., Michigami, K, Wang, B., Komurasaki, K. and Arakawa, Y.: Photoionization in the Precursor of Laser Supported Detonation by Ultraviolet Radiation, AIP Conference Proceedings, **1402**, 326 (2011).
14) Fischer, V. I.: *Soviet Physics: Technical Physics*, **28** (1984).
15) Nielsen, P. E.: Hydrodynamic calculations of surface response in the presence of laser-supported detonation waves, *Journal of Applied Physics*, **46** (1975), pp. 4501-4505.

16) Raizer, Y. P.: Laser-Induced Discharge Phenomenon, Studies in Soviet Science, Consultants Bureau, New York (1977), pp. 199-206.

17) Mori, K., Komurasaki, K. and Arakawa, Y.: Influence of the focusing f number on the heating regime transition in laser absorption waves, *Journal of Applied Physics*, **92**, 10 (2002), pp. 5663-5667.

18) Mori, K., Komurasaki, K. and Arakawa, Y.: Energy transfer from a laser pulse to a blast wave in reduced-pressure air atmospheres, *Journal of Applied Physics*, **95**, 11 (2004), pp. 5979-5983.

19) Mori, K., Komurasaki, K. and Arakawa, Y.: Threshold laser power density for regime transition of a laser absorption wave in a reduced-density air atmosphere, *Applied Physics Letters*, **88**, 121502 (2006).

20) Shimamura, K., Hatai, K., Kawamura, K., Fukui, A., Fukuda, A., Wang, B., Yamaguchi, T., Komurasaki, K. and Arakawa, Y.: Internal structure of laser supported detonation waves by two-wavelength Mach-Zehnder interferometer, *Journal of Applied Physics*, **109**, 084910 (2011).

21) Frisbee, R. H., Horvath, J. C. and Sercel, J. C.: Laser Propulsion for the Orbital Transfer Mission, AIAA Paper 85-1224 (1985).

22) Myrabo, L. N.: Brief History of the Lightcraft Technology Demonstrator (LTD) Project, Beamed Energy Propulsion: First International Symposium on Beamed Energy Propulsion, edited by A. V. Pakhomov, AIP Conference Proceedings, **664** (2002), pp. 49-60.

23) Raizer, Y. P.: *Sov. Phys. JETP*, **21**, 5 (1965), pp. 1009-1017.

24) Shimamura, K.: Ionization kinetics in a laser-supported detonation wave and its propagation limits, *Graduation Thesis*, The University of Tokyo, March 2014, pp. 28-42.

Chapter 2

ELECTRON NUMBER DENSITY AND ELECTRON TEMPERATURE DEDUCTION

2.1 Fundamental Principles of Interferometry

The attainment of the electron number density n_e from basic physical equations is presented. Prior to this, a brief discussion of coherence and the basic mathematical principles of the two-beam interference are presented.

2.1.1 Coherence

Two superimposed beams of light are said to be coherent provided their relative phases are stable for a sufficient period of time to be detected by a sensing system. Coherence is an essential requirement for the formation of an interference phenomenon. For pure temporal coherence, the coherence time t_{coh} is obtained by taking the Fourier transform of the spectral energy distribution of the beam source[1)]. Hence the coherence length l_{coh} as shown in equation (2.1) is the product of t_{coh} and the velocity of light c.

$$l_{coh} = ct_{coh} \tag{2.1}$$

In a focusing plane whose source is a screen with randomly distributed grains with random phase illuminated by a spherical wave; the Fourier transformation of this source area gives the complex degree of pure spatial coherence[2)].

2.1.2 Two-beam interference

A beam of light is a propagating electromagnetic wave. For a scalar or a linearly polarized propagating plane wave in a vacuum, the electric field E at any point can be represented by a sinusoidal function of distance and time as shown in equation (2.2)[3)].

$$E = a\cos\left[2\pi\nu\left(t - \frac{z}{c}\right)\right] \tag{2.2}$$

Where a is the amplitude, ν the frequency, c the speed of wave propagation and z is the distance. The period of vibration T is a function of the angular frequency ω:

$$T = \frac{1}{\nu} = \frac{2\pi}{\omega}\,. \tag{2.3}$$

The wavelength λ is represented as:

$$\lambda = cT = \frac{c}{\nu}\,, \tag{2.4}$$

while the propagation constant of the wave is given by:

$$k = \frac{2\pi}{\lambda}\,. \tag{2.5}$$

In a medium other than vacuum with a refractive index N, the light wave propagates with a speed given by:

$$v = \frac{c}{N}\,, \tag{2.6}$$

and the wavelength of the propagating wave becomes:

$$\lambda_n = vT = v\frac{\lambda}{c} = \frac{\lambda}{N}\,. \tag{2.7}$$

In complex representation, equation (2.2) is of the form:

$$E = \mathrm{Re}\left\{a\exp\left[\mathrm{i}2\pi\nu\left(t - \frac{Nz}{c}\right)\right]\right\}, \tag{2.8}$$

where Re { } is the real part of the complex expression and $\mathrm{i} = \sqrt{-1}$. The right hand side of equation (2.8) can be expressed as a product of the time- and space-varying functions such that:

$$E = \mathrm{Re}\{a\exp(-\mathrm{i}\phi)\exp(\mathrm{i}2\pi\nu t)\}\,, \tag{2.9}$$

$$\phi = 2\pi\nu\frac{Nz}{c} = 2\pi\frac{Nz}{\lambda} = 2\pi\frac{p}{\lambda}\,, \tag{2.10}$$

where ϕ and p are the phase difference and optical path difference respectively. Assuming linearized operations on E, the real part of the complex function can be taken at the final part of the calculation. Thus equation (2.9) is re-written as:

$$E = A\exp(\mathrm{i}2\pi\nu t)\,, \tag{2.11}$$

where

$$A = a\exp(-\mathrm{i}\phi)\,. \tag{2.12}$$

A is the complex amplitude of the wave's vibration. Visible light waves have very high ν of the order of 6×10^{14} Hz for $\lambda = 0.5$ μm. This implies that direct observation of the electric field is impossible and the only measurable quantity is intensity. The intensity, which is proportional to the time average of the square of E, is defined as the time average of the amount of energy, which in a unit of time crosses a unit area normal to the direction of the energy flow[1)]. Mathematically,

$$\langle E^2\rangle = \lim_{T\to\infty}\frac{1}{2T}\int_{-T}^{T}E^2\mathrm{d}t\,. \tag{2.13}$$

Substituting equations (2.2), (2.3) and (2.10) into (2.13), the following equation is obtained.

$$\langle E^2\rangle = \lim_{T\to\infty}\frac{1}{2T}\int_{-T}^{T}a^2\cos^2(\omega t-\phi)\mathrm{d}t = \frac{a^2}{2}\,. \tag{2.14}$$

Since only the relative but not the absolute values over a specified region is of interest, the factor of $1/2$ and any other factors of proportionality can be ignored. Hence the optical intensity is defined as:

$$I = a^2 = |A|^2\,. \tag{2.15}$$

2.1.3 Interference of two monochromatic waves

If two monochromatic waves superposed at a point P, propagate in the same direction and are polarized in the same plane, then the total electric field at P is given as:

$$E = E_1 + E_2 \,. \tag{2.16}$$

E_1 and E_2 are the electric fields of the two waves. If these two waves have the same frequency, then the optical intensity I at this point is

$$I = |A_1 + A_2|^2 \,, \tag{2.17}$$

where

$$A_1 = a_1 \exp(-\mathrm{i}\phi_1) \quad \text{and}$$

$$A_2 = a_2 \exp(-\mathrm{i}\phi_2) \,. \tag{2.18}$$

For intensities at P which are incoherently superposed, we can obtain

$$I = A_1^2 + A_2^2 + A_1 A_2^* + A_1^* A_2$$

$$= I_1 + I_2 + 2\xi_{12}\sqrt{I_1 I_2}\cos(\phi_1 - \phi_2) \,. \tag{2.19}$$

Equation (2.19) is defined as the general interference law for stationary optical fields[2]. For incoherent light, the coherence factor $\xi_{12} = 0$ and for perfectly coherent light, $\xi_{12} = 1$. The maximum intensity $I_{\max}$ is attained when $\phi_1 - \phi_2 = 2m\pi$, m is an integer and the minimum intensity $I_{\min}$ occurs when $\phi_1 - \phi_2 = (2m+1)\pi$. Re-writing equation (2.19) for perfect coherence, we have:

$$I = I_0\{1 + \gamma\cos(\phi_1 - \phi_2)\} \,. \tag{2.20}$$

Where $I_0 = I_1 + I_2$ and γ is the contrast or visibility of the interference fringes given as:

$$\gamma = \frac{(I_{\max} - I_{\min})}{(I_{\max} + I_{\min})} = \frac{2\sqrt{I_1 I_2}}{I_1 + I_2}, \tag{2.21}$$

for which $I_1 = I_2$ for maximum visibility.

Practically, it is very difficult to obtain interference effects with two beams from separate thermal sources, since a thermal source is not purely monochromatic even when it has a single spectral line. This is because, a beam's amplitude and phase have transient and random fluctuations which are not correlated in the case of different sources[3)]. However, it is possible to separate a single source into two beams. The two well established methods for achieving this are wavefront and amplitude divisions. Wavefront division implies using two parts of the source's wavefront. This can be achieved by using an optical system with two mirrors inclined at a small angle with each other such as the Fresnel's mirrors. In amplitude division, the amplitude of the wavefront over the same section is divided. The use of half-silvered mirrors or beam splitters, which transmit a portion of the incident beam and reflect the rest is one of the ways to achieve amplitude division.

In this study, the two beams for the interferogram pattern or fringe formation were obtained from the same source via amplitude division; hence the correlation between the fluctuations of the beams' properties is considered complete and thus completely coherent. For this reason, the basic mathematical principles presented in this section for monochromatic light are sufficient to describe the fringes obtained in this study.

2.2 Mach-Zehnder Interferometry

The Mach-Zehnder interferometer applies the principle of coherence to determine the refractive index of a test section. It basically comprises two beam splitters and two plane mirrors. The first beam splitter separates the beam into the reference beam and the

probe beam. The probe beam is that portion which traverses the test section. The second beam splitter recombines the two beams before exiting the interferometer. It is important that for clear and visible fringe pattern, beams in the opposite arms of the interferometer are parallel with respect to each other. There are two good reasons that make the Mach-Zehnder interferometer an advantageous non-intrusive measurement system. The first is that, the test and reference sections are separated and traversed only once. Secondly, there is much flexibility in fringe localization; thus it is easier to allow the most visible portion of the fringe to coincide with the test section.

2.2.1 Number of fringe shift

The number of fringe shifts in an interferogram is proportional to the sum of the changes in refractive indices along the reference and test sections in the direction of the probe beam. It is given in equation (2.22):

$$h = \frac{1}{\lambda}\int \left(N_{ref}(z) - N_{test}(z)\right) \mathrm{d}z \ , \tag{2.22}$$

where N is the refractive index, z is distance of the test section in the direction of probe beam and the subscripts "ref" and "test" represents the reference and the test section respectively. For a test object with homogeneous characteristics, equation (2.22) can be rewritten as:

$$h = \frac{\left(N_{ref}(z) - N_{test}(z)\right)}{\lambda} \times d = \frac{\Delta N d}{\lambda} \ . \tag{2.23}$$

Here, ΔN and d are the refractive index change and width of the test section in the direction of the probe beam respectively. In this study, $d = 2$ mm.

2.2.2 Relative refractive index

The refractive index of a medium is usually approximated as:

$$N - 1 = \sum K_j n_j \ , \tag{2.24}$$

where K_j and n_j are the relative refractive index and the number density of species j respectively. The medium in this study comprises laser induced plasma which has electrons, ions and neutral particles; and blast wave which has neutral particles. The relative refractive index of an ion and a neutral particle is fairly constant and given as: $K_i = 7.4 \times 10^{-30}\ \mathrm{m}^3$ and $K_n = 1.1 \times 10^{-29}\ \mathrm{m}^3$ respectively. However, the relative refractive index of an electron K_e, is a function of the probe beam's wavelength as shown in Figure 2.1[4].

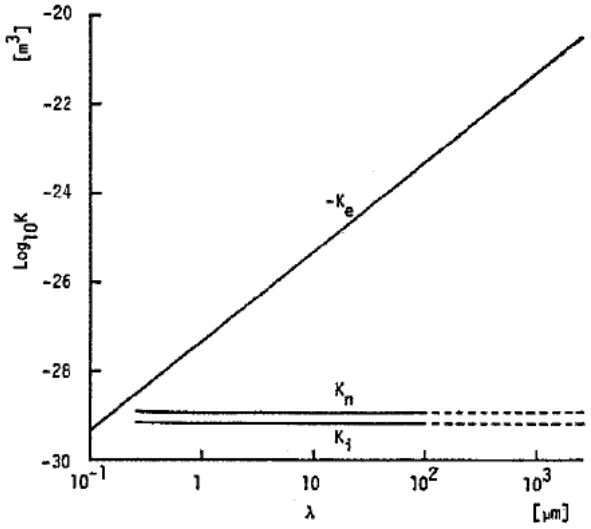

Figure 2.1 The dependence of relative refractive index on wavelength.[4]

K_e can obtained from the dispersion relation of the electromagnetic wave travelling in a plasma under the assumption of no magnetic field. This relation is mathematically defined as[5]:

$$\omega^2 = \omega_{pe}^2 + kc^2 \ , \tag{2.25}$$

from which

$$\left(\frac{kc}{\omega}\right)^2 = 1 - \left(\frac{\omega_{pe}}{\omega}\right)^2 = \epsilon\,. \tag{2.26}$$

k, c, ω and ϵ are the wave number, velocity of light in vacuum, the angular frequency and the dielectric constant respectively. The electron plasma frequency ω_{pe} is given as:

$$\omega_{pe} = \sqrt{\frac{n_e e^2}{m_e \varepsilon_o}}\,, \tag{2.27}$$

where n_e, m_e, e and ε_o are the electron number density, electron mass, electron charge magnitude and permittivity of free space respectively. The refractive index of electron can be defined as:

$$N_e = \frac{kc}{\omega}\,. \tag{2.28}$$

From equations (2.26) and (2.28), we obtain:

$$N_e = \sqrt{1 - \left(\frac{\omega_{pe}}{\omega}\right)^2}\,. \tag{2.29}$$

When the refractive index is not too close to zero, i.e., the plasma density is not too close to the cut-off density n_{co}, then equation (2.29) can be expanded into a Taylor series[6], such that:

$$N_e \approx 1 - \frac{1}{2}\left(\frac{\omega_{pe}}{\omega}\right)^2 = 1 - \frac{1}{2}\frac{n_e}{n_{co}}. \tag{2.30}$$

$$n_{co} = \frac{m_e \varepsilon_o \omega^2}{e^2} \tag{2.31}$$

Combining equations (2.24) and (2.30) and with $\omega = 2\pi c/\lambda$, the relative refractive index of an electron is given as:

$$K_e = -\frac{e^2}{8\pi^2 c^2 m_e \varepsilon_o}\lambda^2\,. \tag{2.32}$$

2.3 Two-wavelength Mach-Zehnder Interferometry

The dependency of K_e on λ and the almost independence of the relative refractive index of heavy particles on λ, makes it possible to deduce the electron number density distribution from two beam sources at different wavelengths. From equations (2.23) and (2.24), we obtain:

$$\Delta N = \frac{h\lambda}{d} = \sum_{ref} K_j n_j - \sum_{test} K_j n_j \,,$$

$$= K_n n_o - (K_n n_n + K_i n_i + K_e n_e) \,, \tag{2.33}$$

where, n_o is the density of neutral particles in the reference path which is usually the atmosphere. The subscripts n, i and e represent neutral particles, ions and electrons respectively.

2.3.1 n_e deduction

When two beams of different wavelengths λ_1 and λ_2 traverses the arms of the Mach-Zehnder interferometer, equations (2.32) and (2.33) describe the changes in the refractive indices due to the two beams as:

$$\Delta N_1 = K_n n_o - K_n n_n - K_i n_i - \left(-\frac{e^2}{8\pi^2 c^2 m_e \varepsilon_o}\lambda_1^2\right) n_e \,, \tag{2.34}$$

$$\Delta N_2 = K_n n_o - K_n n_n - K_i n_i - \left(-\frac{e^2}{8\pi^2 c^2 m_e \varepsilon_o}\lambda_2^2\right) n_e \,. \tag{2.35}$$

The difference of equations (2.34) and (2.35) gives n_e:

$$n_e = \left(\frac{8\pi^2 c^2 m_e \varepsilon_o}{e^2}\right)\left(\frac{\Delta N_1 - \Delta N_2}{\lambda_1^2 - \lambda_2^2}\right). \tag{2.36}$$

Using equations (2.23) and (2.36), the electron number density distribution is obtained.

At the shock front, the number of fringe shifts h is quite difficult to estimate due to the density jump. Considering the fact that at the shock front neutral particles are predominant, the number of concentrated fringes can be obtained from the following relation:

$$h = K_n n_o \left(\frac{\rho_{ref}}{\rho_{test}} - 1\right)\frac{d}{\lambda}\,. \tag{2.37}$$

The density ratio is obtained from the normal shock relation:

$$\frac{\rho_{ref}}{\rho_{test}} = \frac{(\gamma+1)M_{test}^2}{(\gamma-1)M_{test}^2 + 2}\,. \tag{2.38}$$

ρ, γ and M represent density, ratio of specific heats and Mach number respectively. The subscripts "ref" and "test" refer to the reference and test sections of the Mach-Zehnder interferometer.

In this study, the two probe beam colours were blue and infra-red, representing λ of 470 nm and 785 nm respectively. From equation (2.36), it can easily be seen that the pair 470 nm – 785 nm ($n_e = 5.83 \times 10^{27}(\Delta N_{785} - \Delta N_{470})$) increases the detection limit by approximately 13 % compared to 532 nm – 785 nm pair ($n_e = 6.70 \times 10^{27}(\Delta N_{785} - \Delta N_{532})$) used in previous interferometric studies in our laboratory.

2.4 Electron Temperature Deduction

Numerous studies on laser induced plasma have been undertaken via optical emission spectroscopy (OES)[7].The temporal electron excitation temperature distribution was obtained by OES. The intensity and profile of the line emission from the plasma is very important. Three different kinds of line broadening well known are[8),9)]: Natural, Doppler

and Stark broadenings. Natural broadening is as a result of the finite lifetime of excited states and has a Lorentzian profile. Doppler broadening is due to thermal motion of emitting ions and has a Gaussian profile. Doppler broadening is dominant at low electron densities. Stark/ pressure broadening occurs because of the interaction of the emitting ions and the electric field due to plasma electrons and ions. In this study, the Stark broadening was considered dominant because during the LSD regime, the electron number density is very high ($n_e \sim 10^{23}$ m^{-3}). Hence the obtained line spectra from experiment were fitted with the Lorentzian function.

Plasma temperatures are normally determined from the measurement of intensities' ratio of either ion to neutral lines and neutral to neutral lines[10]. Under the assumption that the plasma is both in local thermodynamic equilibrium and optically thin; the electron excitation temperature T_{ex} can be obtained from the Boltzmann plot equation[11]:

$$\ln\left(\frac{I_{ik}}{g_i A_{ik}}\right) = \ln\left(\frac{n_j}{\mathrm{U}_j(T_{ex})}\right) - \frac{E_i}{k_B T_{ex}}\,. \tag{2.39}$$

I_{ik}, g_i, A_{ik} and E_i are the integrated line intensity, statistical weight, transitional probability and excitation energy associated with level i respectively. All four of the atomic spectra parameters are given by the National Institute of Standards and Technology (NIST) database. The subscripts i and k respectively represent the upper and lower levels of energy. n_j, U_j and k_B are the total number density of species j, internal partition function of species j and the Boltzmann constant respectively. It is critical to note that the use of several different line spectra allows greater precision of the plasma temperature determination. This is because the reported values of A_{ik} in literature show a high degree of uncertainty (about 5% - 50%). This uncertainty is "cancelled out" in some sense by the use of many lines[11]. By plotting the left hand side of equation (2.39) versus E_i, the temperature is obtained by comparing $-1/k_B T_{ex}$ to the

slope (from linear regression) of the plot. This does not require the values of the first term on the right hand side of equation (2.39).

References

1) Landolt-Bornstein: Numerical Data and Functional Relationships in Science and Technology, New Series, Group VIII, *Springer-Verlag Berlin Heidelberg*, Volume 1, Subvolume A, Part 2, 2006, pp. 221-228.
2) Born, M., and Wolf, E.: Principles of optics, 6th Ed., *Pergamon Press Oxford*, 1987.
3) Hariharan, P.: Optical Interferometry, 2nd Ed., *Academic Press California*, 2003.
4) Akasaki, M.: *J. High Temp. Soc*., **5**, 235 (1979) (In Japanese).
5) Chen, F. F.: Introduction to Plasma Physics and Controlled Fusion, *Plenum Press New York*, 1974, p. 115.
6) Piel, A.: Plasma Physics: An Introduction to Laboratory, Space, and Fusion Plasmas, *Springer-Verlag Berlin Heidelberg*, 2010, p. 147.
7) Cadwell, L., and Huwel, L.: *Journal of Quantitative Spectroscopy and Radiative Transfer*, **83**, 579 (2004).
8) Griem, H. R.: Plasma Spectroscopy, *McGraw Hill New York*, 1964.
9) Griem, H. R.: Spectral Line Broadening by Plasmas, *Academic Press New York*, 1974.
10) Singh, P. J., and Thakur, N. S. (Editors): Laser-Induced Breakdown Spectroscopy, *Elsevier*, 2007, pp. 83-96.
11) Miziolek, W. A., Palleschi, V., and Schechter, I. (Editors): Laser-induced Breakdown Spectroscopy, Fundamentals and Applications, *Cambridge University Press New York*, 2006, pp. 122-166.

Chapter 3

EXPERIMENTAL APPARATUS

3.1 Laser and Focusing Optics

A transversely excited atmospheric (TEA) CO_2 pulse laser with nominal energy of 10 J was used to produce plasma for the experiments. The laser device is a product of Usho Optical System. Its beam was in the high-order multi-transverse mode. The laser beam's effective diameter and cross-section were 34 mm and approximately 30 × 30 mm squared respectively. The laser gas comprises carbon dioxide, nitrogen and helium; and has a fill pressure of approximately 120 kPa. The nominal energy increases with the fill pressure. A picture of the CO_2 laser and its specification are shown in Figure 3.1 and Table 3.1 respectively. Figure 3.2 shows the variation of the laser pulse energy with the fill pressure in the laser's discharge tube.

Figure 3.1 Picture of the TEA CO2 laser (exterior).

A joule meter was used to measure the pulse energy before and after the experiments. This was to ensure that the shot-to-shot pulse energy deviations were kept below ±5% throughout experimentation. The pulse shape was detected using a photon-drag detector (Hamamatsu photonics-B749). The specification and picture of the detector are shown in Table 3.2 and Figure 3.3 respectively.

Table 3.1 CO2 laser specifications.

Model №	IRL-1201
Nominal energy	10 J
Repetition	single,0.1～0.5 Hz
Gas fill pressure	120 kPa
Output wavelength	10.6 μm
Impressed voltage	~ 10 kV
E_i fluctuation	< ± 5 %
Beam size	30 mm × 30 mm
Power source	AC100V 50／60Hz 3A
Laser gas composition	He: N_2: CO_2 = 84: 8: 8

Table 3.2 Photon-drag detector specification.

Model №	B749
Aperture diameter	5 mm
Sensitivity	1.2 V/MW
Rise time (10 ~ 90%)	< 1 ns

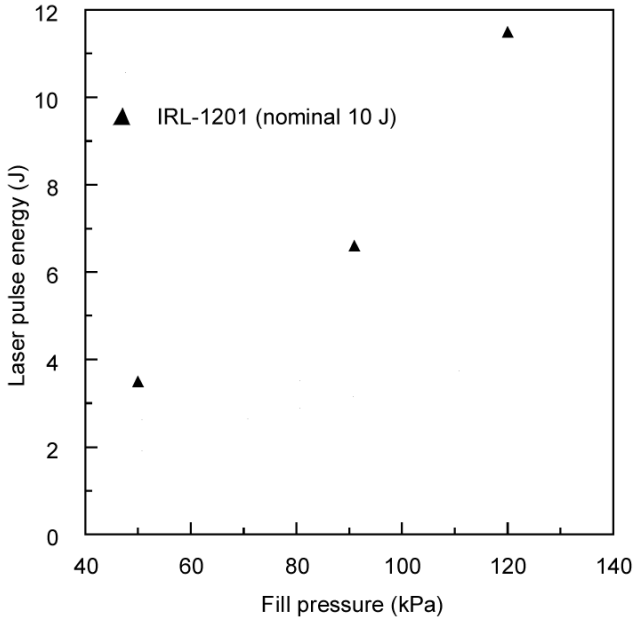

Figure 3.2 Plot of laser pulse energy versus fill pressure.

The laser beam's energy density distribution profile is a flat top hat shape in the horizontal direction and an approximately Gaussian shape in the vertical direction. Figure 3.4 shows the pulse shape of the CO2 laser; which is a leading-edge spike with an exponentially decaying tail. At about 3.5 μs, 95% of the laser energy is discharged. The full width at half maximum was 0.12 ± 0.02 μs for the nominal energy output. The temporal change in the decaying tail power P_{tail}, can be approximately described by the following relation:

$$P_{tail} = P_{o,tail} \exp\left(-\frac{t}{\tau_d}\right), \tag{3.1}$$

where τ_d is the tail decay constant and a function of the fill pressure.

Figure 3.3 Picture of the photon-drag detector.

The laser beam was focused by an off-axis parabolic mirror which has a focal length of 150 mm. The beam is then directed into the experimental chamber after the 90º reflection off the parabolic mirror through a Zinc-Selenide (Zn-Se) window. The laser beam was focused onto an aluminium target plate with two sapphire glasses on each side displaced 2 mm apart. However, no ablation was observed on the surface of the target.

It is very critical to note that the temperature condition of the experiment room was kept at 292 – 295 K, whiles the humidity level remained relatively at 50 – 60%. The pressure level within the test chamber was always 1 atmosphere and was monitored by a kistler pressure gauge.

3.2 Light Sources

As discussed in Chapter 2 of this study, coherence is an essential requirement for the formation of an interference phenomenon. A diode pumped solid-state (DPSS) blue laser (continuous wave (CW), 470 nm, 20 mW) and an infra-red diode laser (CW, 785 nm, 100 mW) were the probe beams for the Mach-Zehnder interferometric study. A spatial filter was used to remove unnecessary multiple-order energy peaks and spatial noise before allowing the beam to traverse the interferometric arms of the experimental apparatus.

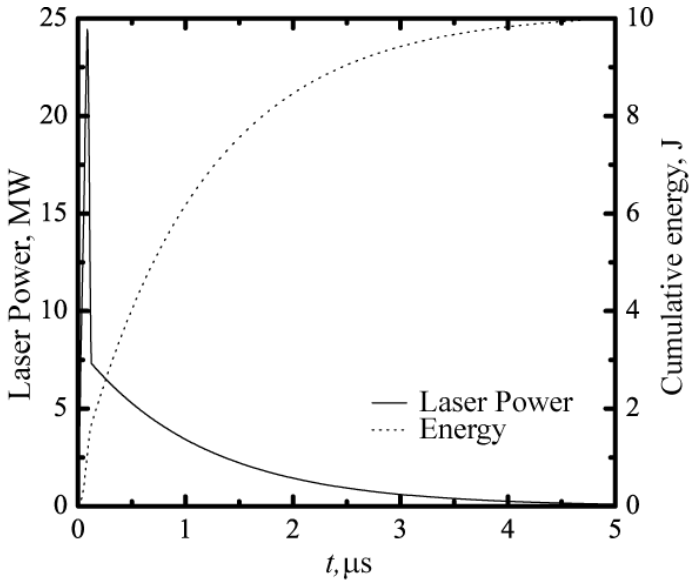

Figure 3.4 Pulse shape of CO_2 laser.

3.3 Imaging Devices

Images and spectrum of the laser induced plasma were taken using two intensified charge coupled device (ICCD) cameras namely; iStar and Ultra 8. The former has a single sequence capability with a higher image resolutions whiles the latter (Ultra 8) is capable of taking eight frames per operation at a maximum rate of 100 million frame per second (FPS). Table 3.3 shows the specifications of both cameras. A pulse delay circuit/generator (Stanford Research Systems, Inc., Model №: DG535, rise time: 2 ns) was used to synchronize the operations of both the CO_2 laser and the ICCD cameras, by receiving an electrical signal from the laser device and transmitting a transistor-transistor logic signal depending on the delay setting to the camera. Figure 3.5 shows an image of the pulse delay generator.

Table 3.3 ICCD cameras specifications.

Product name	iStar	Ultra 8
Company	Andor Technology	DRS Technology
Resolution	1024 × 1024 pixels per frame	520 × 520 pixels per frame
Exposure time	< 2 ns	> 10 ns
Camera sequence	Single	Multiple
Frame per second	Up to 100 million	0.9

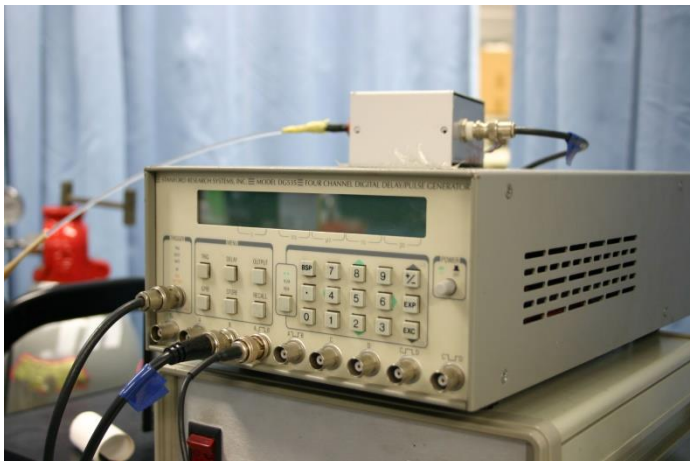

Figure 3.5 Picture of the pulse delay generator.

3.4 Experimental Setup

In this section the constituent devices and equipment as well as their interconnections used in this study are briefly described using schematics and picture images

3.4.1 Interferometry setup

The schematic diagram for the two-wavelength Mach-Zehnder interferometer is as shown in Figure 3.6. The setup was placed on three sets of optical tables which were levelled to ensure that the probe beams were parallel to the horizontal plane containing the setup. This was to ensure the attainment of good coherence for a good fringe pattern. The near-infrared reflector was used to combine both beams into a single path before passing through the spatial filter. The two plano-convex lenses enabled the image of the propagating plasma to be projected visibly onto the ICCD devices.

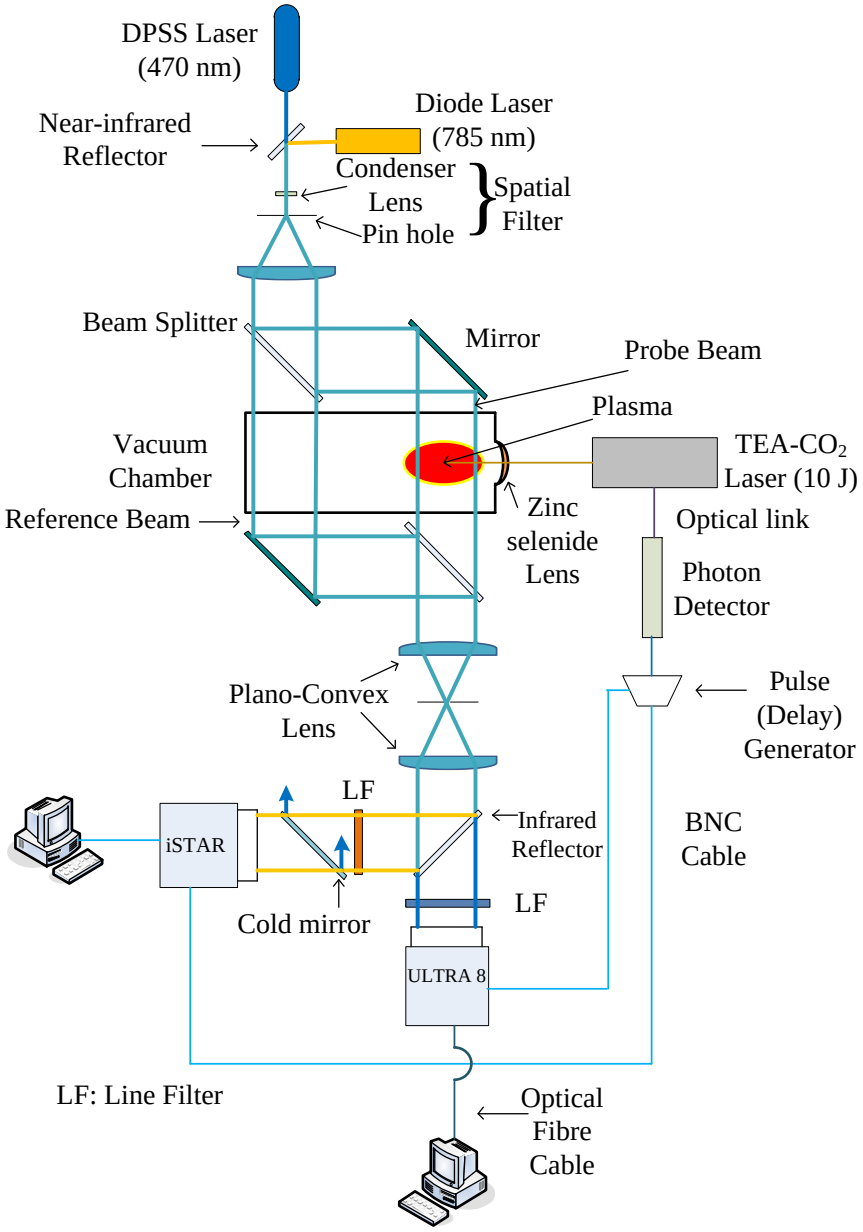

Figure 3.6 Schematic diagram of the 2 wavelength Mach-Zehnder interferometer.

Both ICCD cameras were synchronized to capture the images at the same time using the pulse delay generator. This was verified using an oscilloscope to observe the trigger signals of both cameras. It is also possible to capture the interferograms of both probe beams using a single camera. In this case, both images are juxtaposed side by side on

the detector of the camera. The temporal and spatial resolutions were 100 ns and 10 µm (for blue laser) and 12 µm (for infra-red laser) respectively. Two line filters with specifications: 470 nm ± 10 nm and 785 nm ± 2 nm were used to suppress the plasma emission. The cold mirror was used to filter out any frequency to allow only the 785 nm beam to reach the detector of the ICCD camera. Figures 3.7 and 3.8 show picture images of the probe beam and the interferometric arm sections of the experimental apparatus.

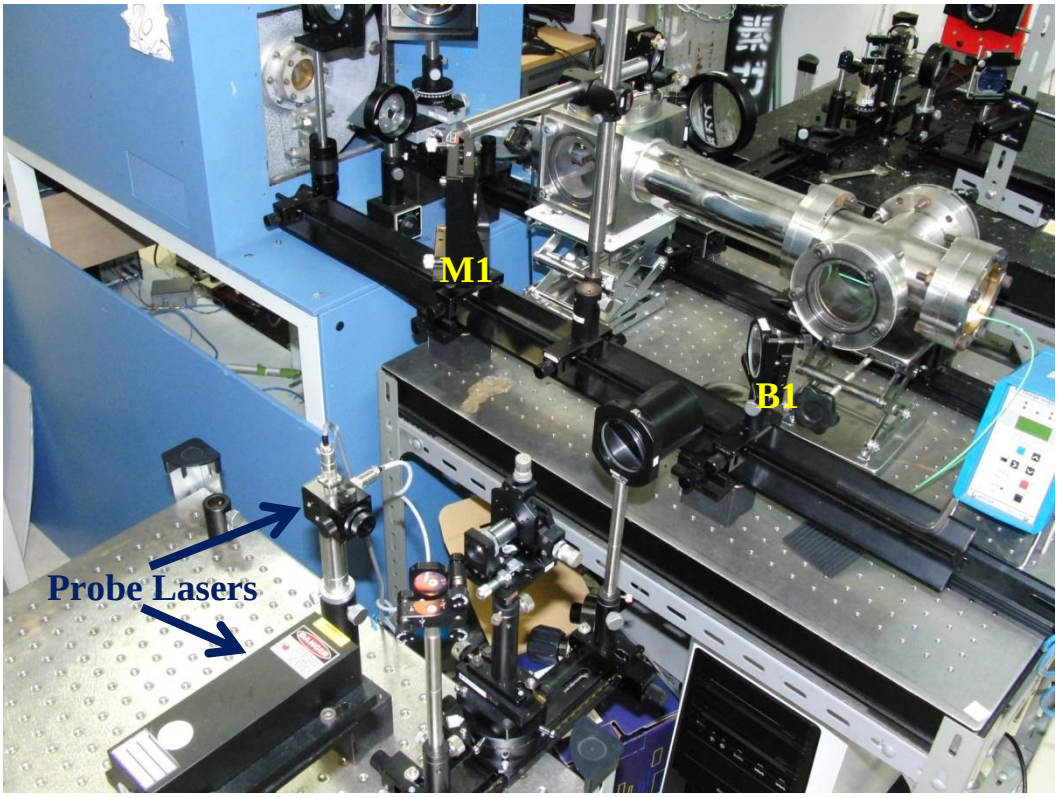

Figure 3.7 Image of the probe beam section of the setup.

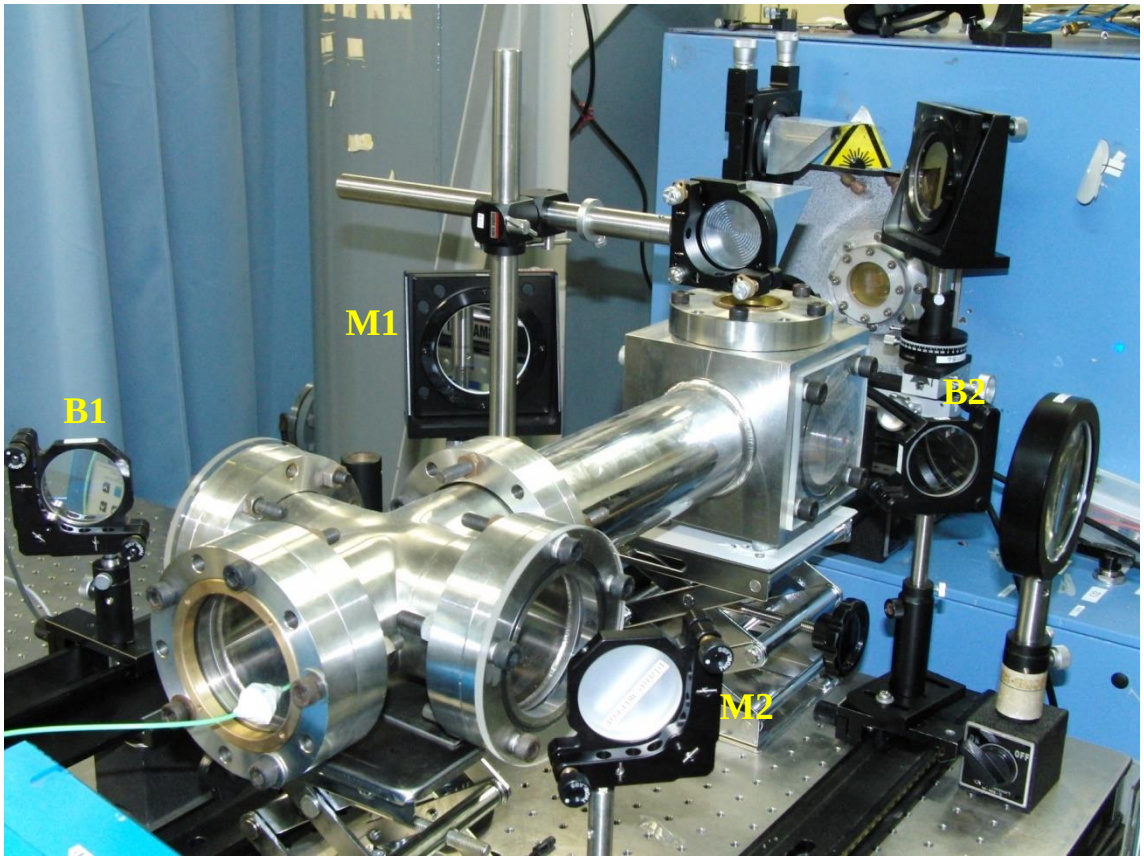

Figure 3.8 Image of the interferometric arm section of the setup.

3.4.2 Spectroscopy setup

The schematic of the optical emission spectroscopy setup is shown in Figure 3.9[1)]. The plasma irradiation was collected using two plano-convex cylindrical lenses of focal length 150 mm and 300 mm respectively. The optical signal was focused into a Czerny-Turner spectrometer (MS3500i, SOL Instruments) coupled with an ICCD camera (iStar, Andor Technology). 50 sets of data were taken per each experimental condition in order to ensure consistency and accuracy of results. The spectrometer shutter exposure time was 100 ns. Table 3.4 gives the specifications of the spectrometer. A xenon lamp (Model № 6033, current: 6 mA, rated operating time: 250 hours) and a halogen lamp were used to calibrate the wavelength and sensitivity respectively.

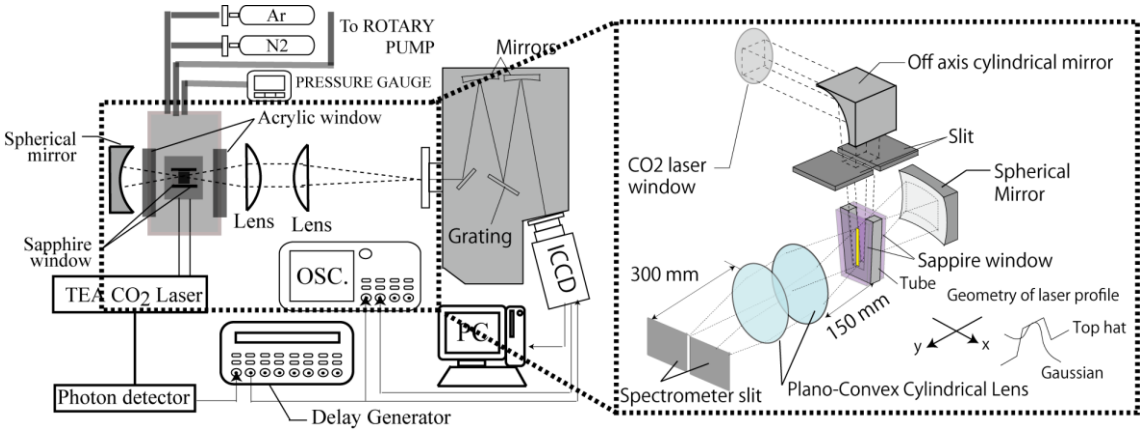

Figure 3.9 Schematic diagram of the spectroscopy setup.[1)]

The spherical mirror placed behind the confinement target was used to reinforce the optical intensity strength from the laser induced plasma. The essence is to increase the signal to noise ratio in order to reduce the exposure time.

Table 3.4 Specifications of spectrometer.

Model №	MS3500i
Company	SOL Instruments
Type	Czerny-Turner
Wavelength range	180 nm – 60 μm
Slit width	0 – 2 mm
Grating size	70 × 70 × 10 mm
f №	3.8

Reference

1) Shimamura, K.: Ionization kinetics in a laser-supported detonation wave and its propagation limits, *Graduation Thesis*, The University of Tokyo, March 2014, pp. 28-42.

Chapter 4

RESULTS AND DISCUSSION

4.1 Experimental Results

In order to predict the velocities of the LSD wave in Ar and N_2 using the 1-D radiative model[1], it was important to obtain the electron number density n_e and the excitation temperature T_{ex} at pre-termination LSD time. Thus n_e and T_{ex} for both gases were obtained at 1.4 µs, although the LSD wave termination time was 1.6 µs and 1.4 µs respectively in Ar and N_2.

4.1.1 n_e deduction

Figure 4.1 shows a sample of the interferogram taken at 1.4 µs for both the 470 nm and 785 nm beams. In order to obtain the change in refractive index ΔN in each probe beam, the fringe shifts must be obtained.

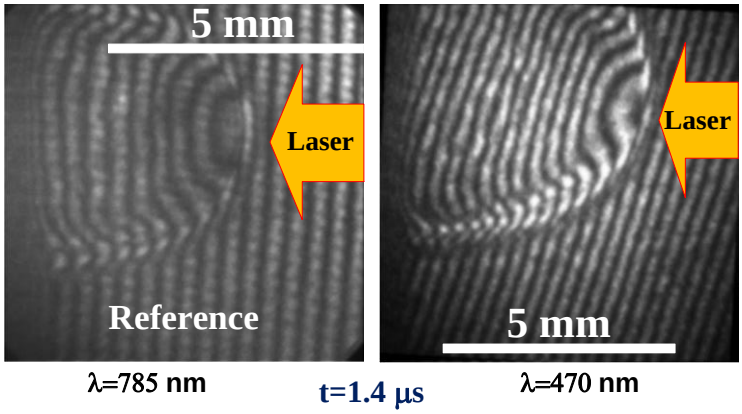

Figure 4.1 Sample interferogram image taken at 1.4 µs.

After denoising the interferogram using a 2D FFT filter, the number of fringe shifts h was deduced by analysing the intensity profile of the interference pattern along the axis of the interferogram. This was attained by comparing the shifted interference pattern with the reference (non-shifted) pattern. A typical example of intensity profiles of both

reference and shifted sections are shown in Figures 4.2(a) and (b) respectively. At the shock front, equations (2.37) and (2.38) were used to estimate h.

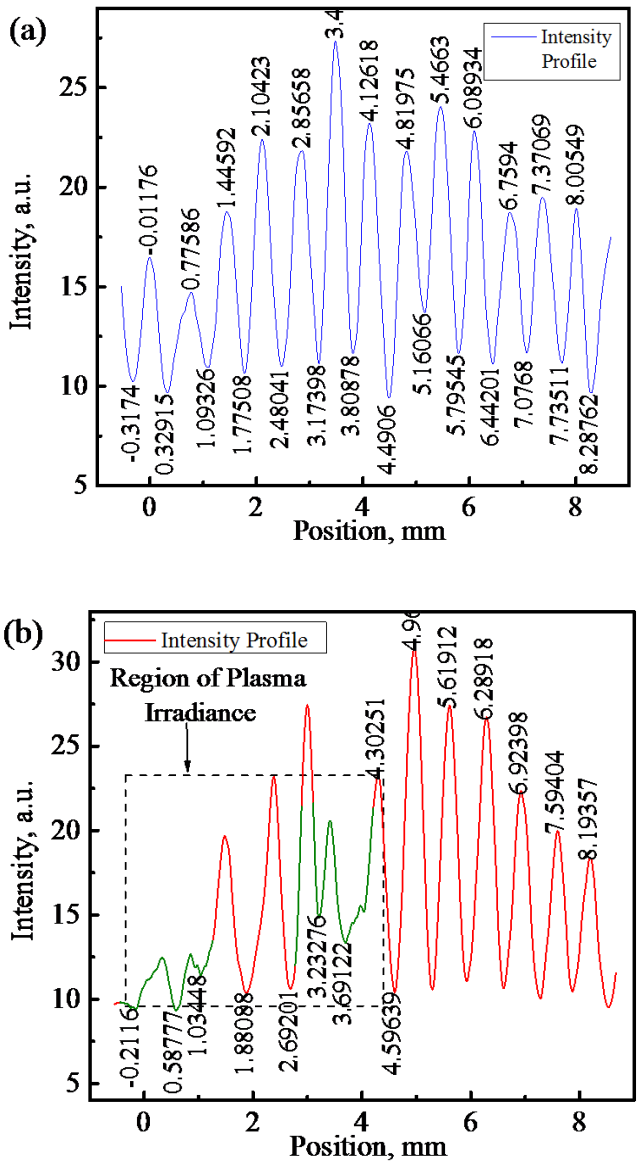

Figure 4.2 Intensity profiles of: (a) reference section, (b) shifted section.

The obtained ΔN in both probe beams was used in equation (2.36) to profile the electron number density. Figures 4.7 and 4.8 show the n_e profiles for Ar and N_2 respectively.

4.1.2 T_{ex} deduction

Figures 4.3 and 4.4 show samples and fitted results of Ar II and N II lines respectively obtained during the spectroscopic experiment. The ionic lines were observed in the range of 455 nm – 485 nm, and were taken at 1.4 μs at a position of 3 mm from the base of the aluminium target. The lines were fitted by the Lorentzian function, and the sum of the fitted lines shows good agreement with the observed lines.

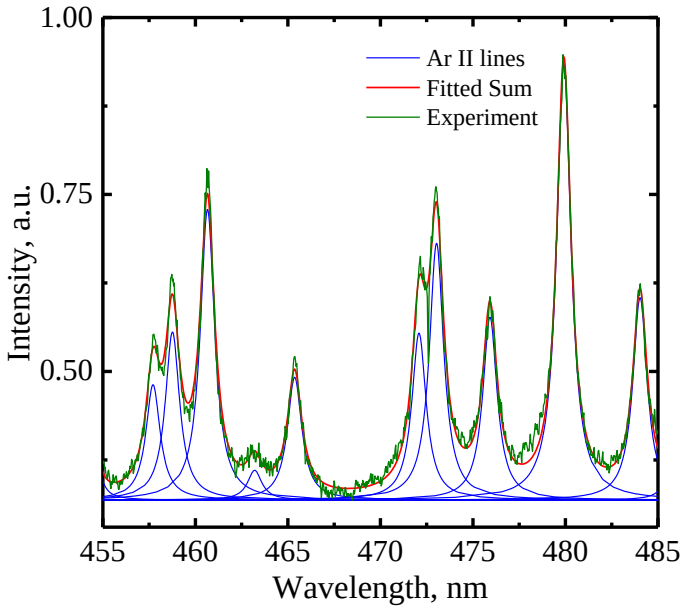

Figure 4.3 Observed and fitted Ar II lines at 1.4 μs.

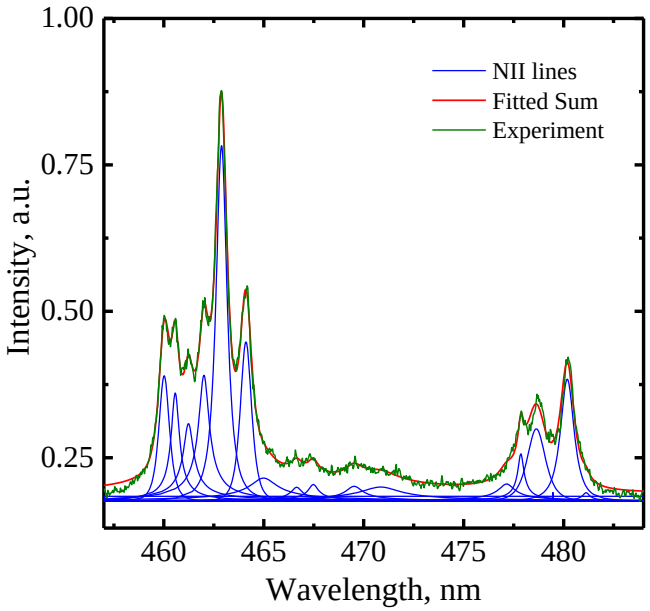

Figure 4.4 Observed and fitted N II lines at 1.4 μs.

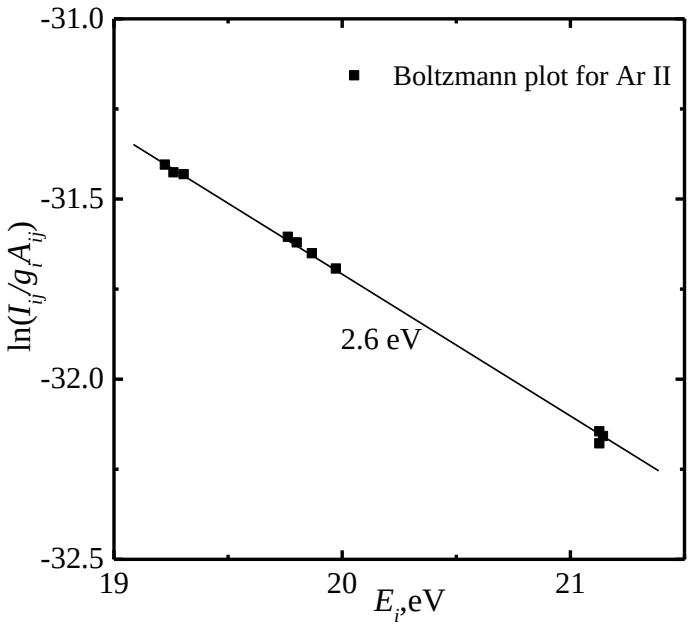

Figure 4.5 Boltzmann plot for Ar II lines at 1.4 μs and 3 mm upstream from the target.

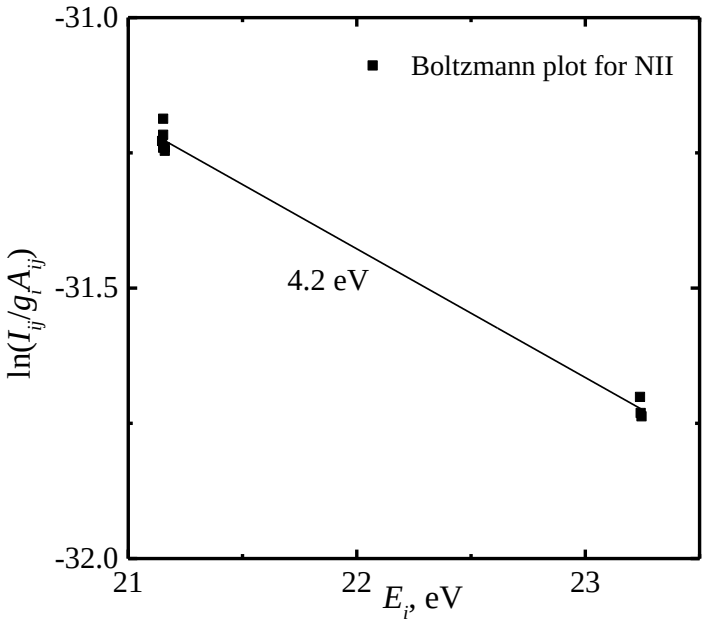

Figure 4.6 Boltzmann plot for N II lines at 1.4 μs and 3 mm upstream from the target.

Figures 4.5 and 4.6 show the Boltzmann plots for Ar II and N II lines at an elapsed time of 1.4 μs. The measured position was 3 mm upstream from the base of the aluminium target. The plots were attained using the NIST database[2] $[A_{ik}, E_i, g_i]$ and the Boltzmann plot equation (equation (2.39)). Tabulated in Table 4.1 are the parameters for Figure 4.6.

Table 4.1 Boltzmann plot parameters for N II.

λ, nm	$A_{ik}, 10^7 \mathrm{s}^{-1}$	E_i, eV	g_i
460.15	2.22	21.160	5
460.70	3.15	21.153	3
461.40	2.12	21.153	3
462.14	9.04	21.148	1
463.05	7.48	21.160	5
464.33	4.39	21.153	3
477.97	2.49	23.240	3
478.82	2.5	23.242	5
480.36	3.17	23.246	7

The obtained electron excitation temperature for Ar and N_2 gases are plotted in Figures 4.7 and 4.8 respectively. Table 4.2 shows the peak values of n_e and T_{ex} in the plots.

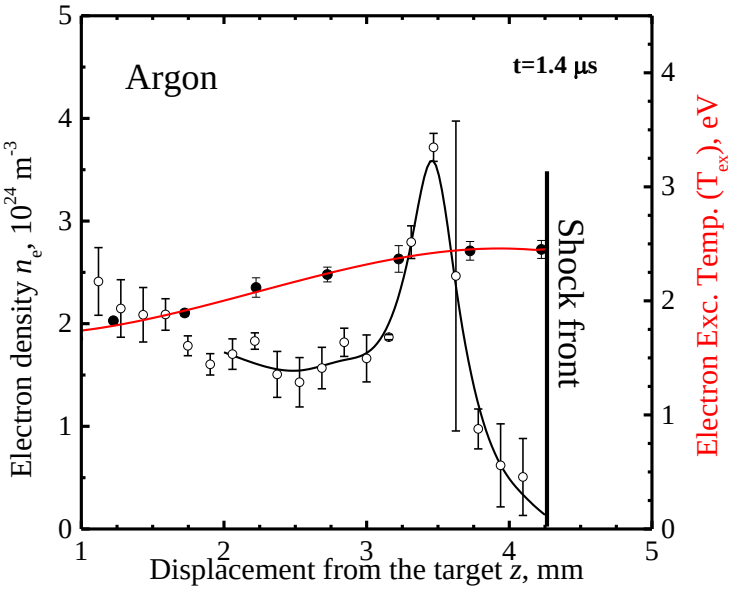

Figure 4.7 n_e and T_{ex} profiles of Argon at 1.4 μs.

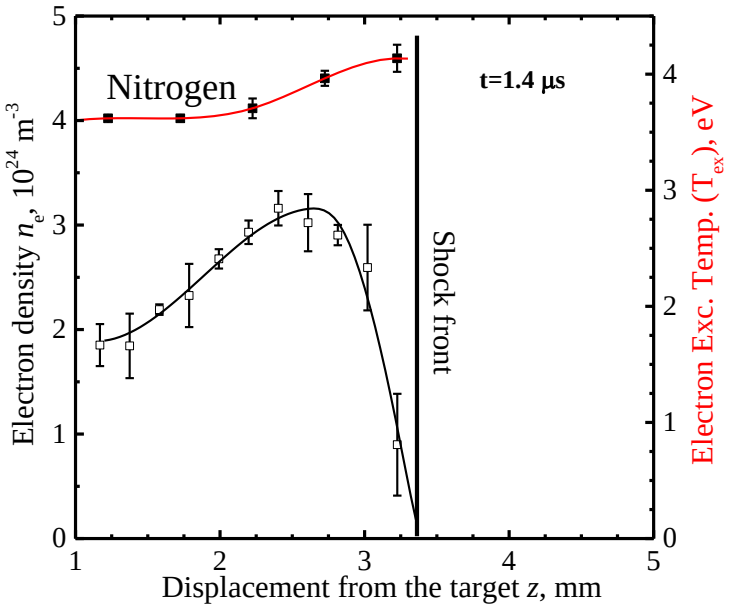

Figure 4.8 n_e and T_{ex} profiles of Nitrogen at 1.4 μs.

Table 4.2 Peak n_e value and maximum T_{ex}.

n_e & T_{ex}	Argon	Nitrogen
Peak n_e, $10^{24}\mathrm{m}^{-3}$	3.23 ± 0.14	3.16 ±0.27
$T_{ex,max}$, eV	2.44 ± 0.13	4.60 ± 0.13

From the above table and the respective plots, the electron number density distribution is almost similar in both gases, however, the maximum excitation temperature for N_2 gas is about twice that of Ar gas.

4.2 Estimated Results

The 1-D radiative hydrodynamic model[1)] uses the conservation equation of n_e as defined for the streamer head expansion in the electric field by Raizer[3)]. The equation is presented in equation (4.1) and the solution for the ionization wave velocity U when the partial time derivative term is neglected, is given in equation (4.2).

$$\frac{\mathrm{d}n_e}{\mathrm{d}t} = \frac{\partial n_e}{\partial t} - U\frac{\partial n_e}{\partial z} = \nu_i n_e \,, \tag{4.1}$$

where, ν_i is the ionization frequency and

$$U = \frac{\nu_i |z_f - z_p|}{\ln\left(n_e(z_p)/n_e(z_f)\right)} \,. \tag{4.2}$$

$n_e(z_p)$ and $n_e(z_f)$ are the electron number densities at the peak and ahead of the shock front positions respectively along the axis of the plasma and precursor region. The qualitative distribution of the electron number density distribution is shown in Figure 4.9[1)]. $n_e(z_f)$ is not easily determined from experiments and thus can be obtained from the relation expressed by equation (4.3):

$$n_e(z_f) = \frac{\phi}{U}\,. \tag{4.3}$$

Hence U can be obtained from solving both equations (4.2) and (4.3). The flux of the UV radiation from the plasma, ϕ can be obtained from equation (4.4)

$$\phi = \int_0^z \int_{v_i}^{\infty} \int_0^{\theta} \left(\frac{I}{hv_i}\right) dz dv d\Omega\,, \tag{4.4}$$

here Ω is the solid angle defining the propagation direction.

For a detailed discussion on how to obtain the radiated power per unit volume I and ϕ, please refer to reference 1) of this chapter. Figure 4.10 explains how ϕ and $n_e(z_f)$ were estimated. z_f is the position of first avalanche ionization and the distance between z_ϕ and z_f defines the integrated n_e contributing to ϕ (total number of photons per unit area per second) at z_f. This distance (depicted by the shaded region) is 1 order higher than the mean free path of photon-absorption λ_{mfp}. The total optical intensity I was estimated considering the radiation due to the free-free and the free-bound transitions as well as the attenuation within the plasma. The proportional relation is as shown below:

$$I \propto i_\nu \left(1 - \exp\left(-\kappa L(\theta)\right)\right)\,,$$

Where κ is the photon-absorption coefficient and i_ν is the radiation due to free-free and free-bound transitions. ϕ was estimated using equation (4.5) considering a simple 1-D case and assuming that half of the total plasma radiation went in both directions along z.

$$\phi = 2\pi \iint \left(\frac{I}{hv_i}\right) dz dv \tag{4.5}$$

Using the values of Table 4.2 which are obtained experimental results, ϕ was computed to be 1.96×10^{24} $m^{-2}s^{-1}$ and 17.3×10^{24} $m^{-2}s^{-1}$ respectively in Ar and N_2. The measured and estimated U in Ar were 1038.92 ms^{-1} and 1495.09 ms^{-1} whiles those of N_2 were

1030 ms^{-1} and 1521.88 ms^{-1} accordingly. Table 4.3 shows the computed generated seed electron number density at the 1.4 μs time for both Ar and N_2 gases. This depicts the effect of electron excitation temperature on seed electron generation via photon flux radiation. Figure 4.11 shows the plot of estimated and measured ionization front speeds within the region of interest versus laser intensity.

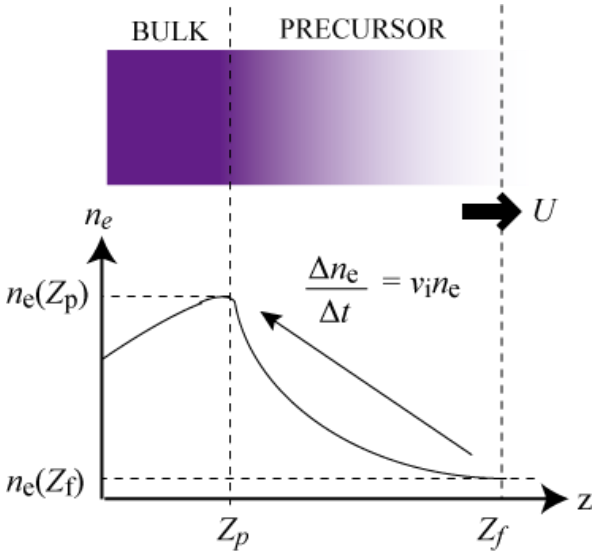

Figure 4.9 Qualitative distribution of n_e.[1)]

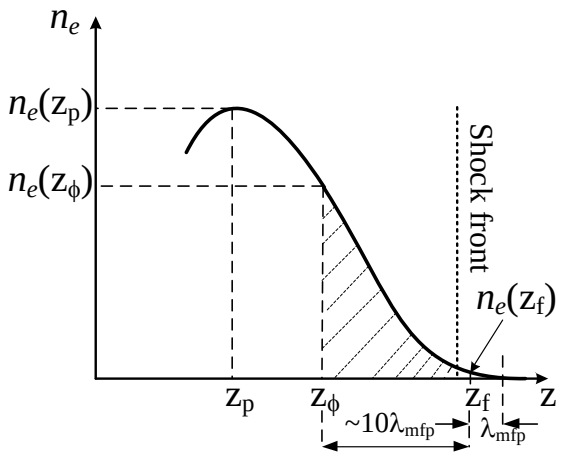

Figure 4.10 Estimation of photon flux, ϕ.

Table 4.3 Measured and estimated parameters at 1.4 µs.

Parameters	Argon	Nitrogen
Measured z_p, 10^{-4} m	8.5	7.0
Computed $n_e(z_f)$, 10^{22} m^{-3}	0.13	1.14
Computed ϕ, 10^{24} $m^{-2}s^{-1}$	1.96	17.3
Estimated U, ms^{-1}	1495.09	1521.88

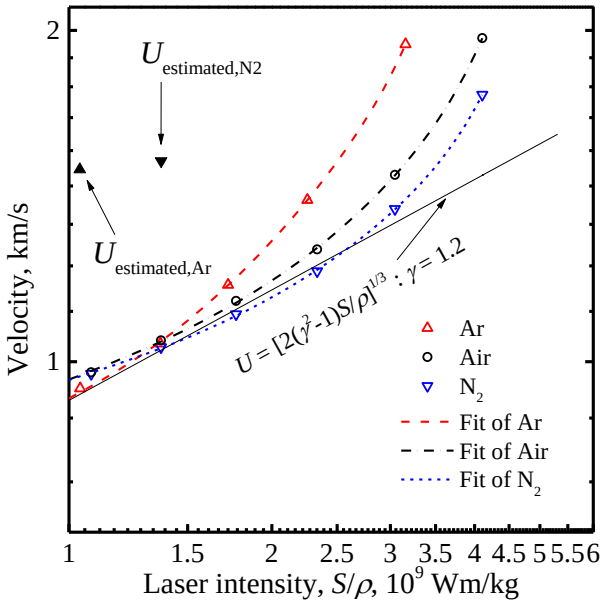

Figure 4.11 Measured and estimated velocities versus laser intensity.

4.3 Discussion

Assuming the existence of doubly ionized Ar species and considering the fact that N_2 has a high probability of dissociating before being ionized, then the order of n_e is expected to be same in both Ar and N_2. At the same laser intensity, the energies required to achieve Ar^{++} (~43 eV) and N^+ (~40 eV) are almost similar and is shown in the simplified energy diagram of Figure 4.12. The ionization processes to obtain Ar^{++} and N^+ are as shown below:

$$\left.\begin{array}{l} \mathrm{Ar} + e^- \Rightarrow \mathrm{Ar}^+ + 2e^- \\ \mathrm{Ar}^+ + e^- \Rightarrow \mathrm{Ar}^{++} + 2e^- \end{array}\right\}, n_e \sim 4e^-$$

$$\left.\begin{array}{r} \mathrm{N_2} \Rightarrow \mathrm{N} + \mathrm{N} \\ \mathrm{N} + e^- \Rightarrow \mathrm{N}^+ + 2e^- \\ \mathrm{N} + e^- \Rightarrow \mathrm{N}^+ + 2e^- \end{array}\right\}, n_e \sim 4e^-$$

The above shows avalanche ionization processes. These processes could be possibly achieved by photoionization, thus e^- could be replaced by $h\nu$.

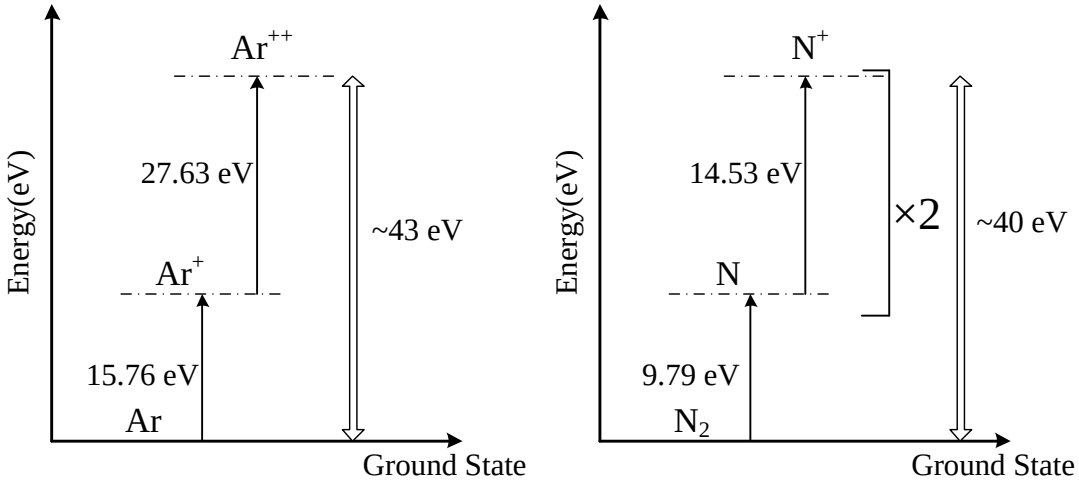

Figure 4.12 Simplified energy diagrams of Ar and N_2.

Table 4.4 shows the heat deposition q and displacement z in both gases at an elapsed time of 1.4 μs.

Table 4.4 q and z at 1.4 μs.

Parameter	Gas	
	Ar	N_2
q, $MJkg^{-1}$	1.30	1.11
z, mm	4.25	3.36

At 1.4 μs $T_{ex,\mathrm{N_2}} \cong 2T_{ex,\mathrm{Ar}}$, and this is so per the assumption that heat absorbed in N_2 is used for plasma heating whiles heat deposited in Ar adds up to the kinetic energy of

plasma particles. This possibly explains why Ar was farther displaced than N_2 at the same time with similar q.

Photon flux ϕ is a function of n_e and T_{ex}. The n_e distribution and peak values were similar in both Ar and N_2, however the maximum electron excitation temperature T_{ex} in N_2 was twice that of Ar. This implies a higher radiative energy (photon flux ϕ) in N_2 than in Ar and this translates into a higher rate of seed electron generation in N_2 than in Ar at t= 1.4 µs. Thus per the 1-D radiative model, estimated *U* is expected to be relatively faster in N_2 than in Ar.

References

1) Shimamura, K.: Ionization kinetics in a laser-supported detonation wave and its propagation limits, *Graduation Thesis*, The University of Tokyo, March 2014, pp. 28-42.

2) (Online). NIST Atomic Spectra Database, http://physics.nit.gov.

3) Raizer, Y. P.: Laser-Induced Discharge Phenomenon, Studies in Soviet Science, Consultants Bureau, New York (1977), pp. 199-206.

Chapter 5

CONCLUSION

Experimentally obtained LSD velocity profiles of Ar and N_2 were compared with that estimated from a 1-D radiative hydrodynamic model. The model predicted the LSD wave velocities precisely in terms of tendency but not accurately. This is due to the dimensional, translational ionization frequency and molecular ionization assumptions of the model. The model estimates parameters of a 2-D experiment and its ionization frequency excludes vibrational and rotational processes.

The computed flux and corresponding estimated front seed electron generation in both Ar and N_2 further validates the applicability of the model to other gases by corroborating measured results.

The phenomenon within the region of high heat deposition requires further experiment and computational analyses for the explanation of its occurrence. This is considered as a future work of this thesis.

Academic Publications

Journal Publication

K. Shimamura, K. Komurasaki, J. A. Ofosu, and H. Koizumi, Precursor ionization and propagation velocity of a laser-absorption wave in 1.053 and 10.6 μm wavelengths radiation, *IEEE Transactions on Plasma Science*, (2014).(Accepted).

Conference Proceedings

International

[1] K. Shimamura, J.A. Ofosu, M. Fukunari, K. Komurasaki, A weak-overdriven detonation mode for laser-produced plasma, P3-39, IEEE Pulsed Power & Plasma Science, San Francisco, California, USA (2013).

[2] K. Shimamura, J.A. Ofosu, M. Fukunari, H. Koizumi, K. Komurasaki, Radiation structure of laser-produced plasma at low mach-number by 2-wavelength Mach-zehnder interferometer,P3-36, IEEE Pulsed Power & Plasma Science, San Francisco, California, USA (2013).

[3] K. Shimamura, J.A. Ofosu, K. Komurasaki, Influence of the self uv-radiation on the structure of the laser-supported detonation wave, 2013-b-25, 29th International Symposium on Space Technology and Science, Nagoya, JPN (2013).

[4] K. Shimamura, K. Michigami, J. A. Ofosu, K. Komurasaki, Influence of the gaseous form on the precursor heating layer of a laser-supported detonation wave using half self-emission half shadowgraph visualization, DPP12-2012-000069, 54th Annual Meeting of the APS Division of Plasma Physics, Rhode island, U.S.(2012). ABSTRACT PPT

[5] J. A. Ofosu, “Characterization of Laser-supported detonation density profile using two-wavelength Mach-Zehnder Interferometer,” 29th International Symposium on Space Technology and Science, Nagoya, June 3-7, 2013.

Domestic

[1] 嶋村耕平、ジョセフ・オフォス,小紫公也 レーザーデトネーションの伝播構造に関する実験的研究 日本航空宇宙学会第 44 期年会講演会, A13, 本郷, 2012 年 4 月 （口頭発表)

[2] 嶋村耕平、ジョセフ・オフォス,小紫公也 自己輻射がレーザーデトネーションの伝播に与える影響 平成 24 年度衝撃波シンポジウム, 1A1-4, 小倉, 2013 年 3 月 （口頭発表)

[3] 嶋村耕平、ジョセフ・オフォス,小紫公也 レーザーデトネーションの自己輻射がその伝搬に与える影響 第 53 回航空原動機・宇宙推進講演会, JSASS-2013-0032, 倉敷, 2013 年 3 月 （口頭発表)

[4] 嶋村耕平、ジョセフ・オフォス,小紫公也 レーザーデトネーションにおける自己輻射と先駆電離層に関する考察, 平成２４年度宇宙輸送シンポジウム, STEP-2012-017, 相模原, 2013 年 1 月 （口頭発表)

[5] ジョセフ・オフォス,嶋村耕平、小紫公也、小泉宏之、荒川義博 Influence of gas type on internal structure of laser supported detonation using 2-wavelength Mach-Zehnder interferometer, 第 56 回宇宙科学技術連合講演会 , 3J19, 別府, 2012 年 11 月 （口頭発表)]

[6] J. A. Ofosu, K. Shimamura, K. Komurasaki, H. Koizumi, “Influence of gaseous media on laser-detonation wave by 2-wavelength Mach-Zehnder interferometry,”

Proceedings of the 57th Japan Society for Aeronautical and Space Sciences Conference, Yonago, Tottori, October 09-11, 2013.